

# Segmented and shielded structures for reduction of thermal expansion-induced tilt errors

Anastasios John Hart<sup>a,\*</sup>, Alexander Slocum<sup>a</sup>, Jason Sutin<sup>b</sup>

<sup>a</sup> *Department of Mechanical Engineering, Precision Engineering Research Group, Massachusetts Institute of Technology, 77 Massachusetts Avenue, Room 3-470, Cambridge, MA 02139, USA*

<sup>b</sup> *Department of Physics, Laboratory for Fluorescence Dynamics, University of Illinois at Urbana-Champaign, USA*

Received 19 February 2003; received in revised form 20 November 2003; accepted 22 January 2004

## Abstract

The design and prototype tests of a segmented and shielded instrumentation structure, based on tube modules connected by canoe ball type kinematic couplings, are presented with application to a high-precision microscope for biological science experiments. The segmented tube design is shown to be significantly less sensitive to deformation from uneven thermal disturbances than a single tube structure. The gaps between the tube segments relieve thermal strains and restrict axial heat conduction, and the large-radius kinematic couplings provide high thermal resistance interconnects without significantly degrading structural stiffness. Simulation results, based on two- and three-dimensional models of heat conduction, are verified with experimental measurements of prototype structures and are used to predict the dependence of the tilt error on the geometry, boundary conditions, and material properties of the tubular segments. Adding layers of low-cost foam insulation and thin metal shielding to the walls of the structure further improves performance. Kinematic couplings could allow the structure to be disassembled and reassembled without re-calibration, and thus, pre-calibrated tube modules with different components could be easily and quickly interchanged between experiments.

© 2004 Elsevier Inc. All rights reserved.

*Keywords:* Thermal expansion; Microscope; Structure; Tilt errors; Kinematic coupling; Infinity-corrected

## 1. Introduction

Technological advances in lasers, detectors, data acquisition electronics, and computer processing have revolutionized the use of optical microscopy in biology. The trend in microscopy is towards greater precision and more quantitative experiments. Microscopes are now used for a wide variety of tasks in addition to imaging, requiring complex laser optics, metrology tools, and precision motion mechanisms in conjunction with the basic microscope structure. Increased interest in single molecule detection and analysis is driving measurements to sub-nanometer resolution. However, structural designs of current microscopes, which have retained similar cantilevered shapes for decades, make such advanced setups cumbersome and sensitive to thermal and mechanical disturbances. The mechanical performance of the microscope has become the limiting factor for many high-resolution experiments.

The High Precision Microscope (HPM) project, a collaboration between the University of Illinois Laboratory for Fluorescence Dynamics and the MIT Precision Engineering Research Group, is developing a novel microscope system to address the needs of multi-mode, quantitative biological experiments. A modular, symmetric cylindrical design was chosen for the HPM body, as shown conceptually in Figs. 1 and 2. Each of the modules is independent and contains a particular set of optics and mechanics for a specific task. Within the module, the components are mounted to the inside of the cylindrical structure. The modules are connected by canoe ball kinematic couplings, which maintain the optical alignment of the microscope while allowing the microscope to be reconfigured with different arrangements of the modules.

By integrating the optical design with the mechanical design, we have created a mechanical structure which efficiently channels disturbances into optically insensitive degrees of freedom. Thus, while disturbances such as thermal expansion cannot be completely eliminated, their effects on the performance of the microscope can be greatly by exploiting the detailed functions of the optical design. Adjusting both the mechanical and optical design ensure that mechanical

\* Corresponding author. Tel.: +1-617-258-8541; fax: +1-617-258-6427.

E-mail address: [ajhart@mit.edu](mailto:ajhart@mit.edu) (A.J. Hart).

URL: <http://pergatory.mit.edu>.

**Nomenclature**

$A$	area of conduction cross-section
$b$	width of rectangular plate model of tube segment
$c_p$	material heat capacity per unit mass
$d$	transient thermal penetration depth of temperature change
$d_{cr}$	critical dimension for segmentation under constant heat source
$D$	diameter (at center of segment wall thickness) of tube stack
$f_T$	focal length of tube lens
Fo	Fourier number
$h$	height of tube segment
$h_a$	heat transfer coefficient between segment wall and ambient
$h_e$	heat transfer coefficient between segment edges and ambient
$H$	height of tube stack
$I_0$	zeroth-order Bessel function $I$
$I_1$	first-order Bessel function $I$
$k$	tube material thermal conductivity
$k_{ins}$	insulation material thermal conductivity
$k_{sh}$	shield material thermal conductivity
$K_0$	zeroth-order Bessel function $K$
$K_1$	first-order Bessel function $K$
$L$	length of conduction body
$L_s$	distance along tube stack from objective location to top plate
$M_o$	magnification of microscope objective
$Q$	power of heat source
$r$	radial coordinate of circular plate
$R$	radius (at center of segment wall thickness) of tube stack
$R_b$	radial location of heat source on circular plate
$R_c$	radial location of outer edge of circular plate
$t$	time
$T$	temperature
$T_b$	temperature at heat source of circular plate
$T_h$	temperature of heated side of tube stack
$T_n$	temperature of non-heated side of tube stack
$T_w$	ambient temperature
$w$	thickness of tube segment
$w_{ins}$	thickness of insulation
$w_{sh}$	thickness of outer metal shielding
$z$	vertical coordinate along tube stack, starting at the bottom of the stack
$Z_a$	dimensionless radial location of heat source on circular plate
$Z_b$	dimensionless radial location of outer edge of circular plate

**Greek symbols**

$\alpha$	material thermal diffusivity
$\alpha_t$	material coefficient of thermal expansion
$\beta$	dimensionless temperature of circular plate
$\delta$	differential expansion between sides of tube stack
$\delta_{obj}$	displacement at the objective position of the tube stack
$\theta_{tilt}$	tilt angle of top plate of tube stack
$\rho$	material density
$\zeta$	dimensionless radial coordinate of circular plate

disturbances are complementary to optical sensitivities is a powerful means to extend the performance of the microscope beyond what is achievable by minimizing the disturbances alone. This paper focuses on modeling and measurement of thermal expansion-induced tilt errors of the HPM structure.

**2. Microscope structure design**

Modern microscopes contain multiple distinct lens units along multiple paths separated by distances of hundreds of millimeters or more. Infinity-corrected optics are used to flexibly and efficiently couple light from the microscope objective (the lens unit closest to the sample under observation) with the different lens groups further along the microscope structure. In an infinity-corrected microscope, light enters and leaves the back aperture of the microscope objective in

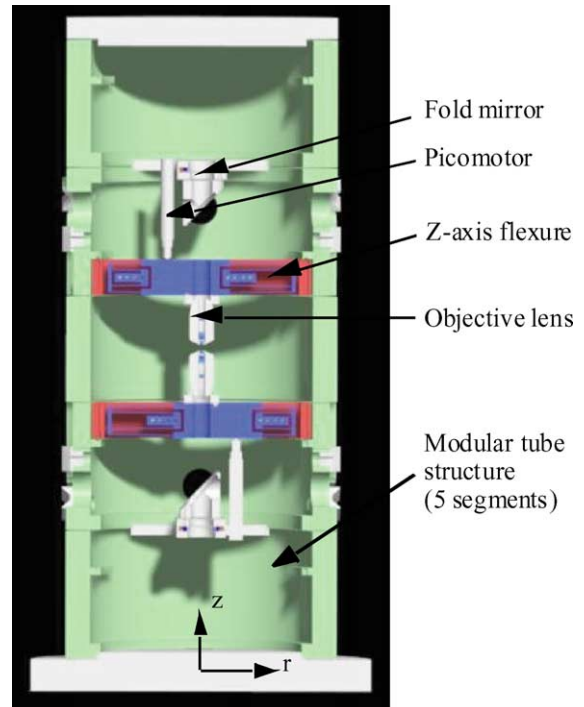


Fig. 1. Cross-section of solid model of high precision microscope (HPM) concept. Sample stage between the two objectives is not shown.

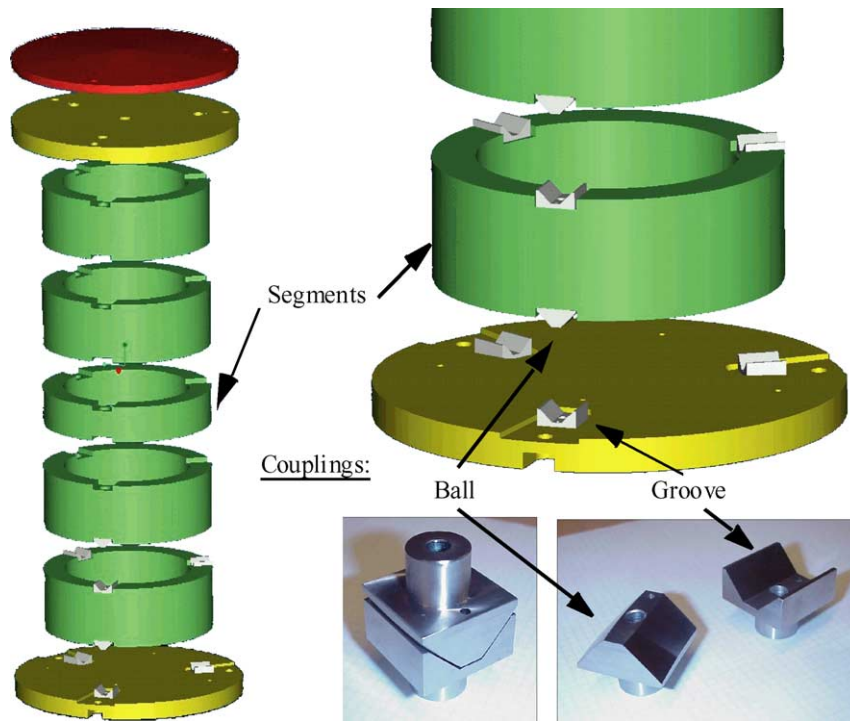


Fig. 2. Exploded view of solid model of tube assembly (only bottom layer of kinematic couplings shown) and prototype stainless steel canoe ball kinematic couplings.

parallel ray bundles, as shown in Fig. 3, facilitating transport of light over long distances [1]. The main advantage of using infinity-corrected optics is that the distance between the lens units in the infinite conjugate space of the microscope has no effect on the measurement (in the absence of beam clipping) since the rays are parallel. This allows many optical units to be easily inserted, each independent of the other, into the infinity space of the optical path. For the HPM structure design, the infinity space provides an optically insensitive axis of expansion.

The light at the back aperture and the light at the sample plane are related by the Fourier transform. Thus, ray bundles entering the back aperture at different angles are focused to

different positions in the sample plane. Likewise, rays at different positions in the back aperture are mapped to different focusing angles in the sample plane. Thus, lateral translation of the objective, relative to other optics in the infinity space path, does not change the position of the illuminated volume in the sample or the detected image from the sample. Translation of the objective will change the zone through which light will travel through the lenses and the angle through which it impinges on the sample, however this has a much smaller, second-order effect on most microscope measurements. Therefore, the most sensitive degrees of freedom for the infinity-space optics are the two axes of tilt perpendicular to the optical axis, which generate translation of the fo-

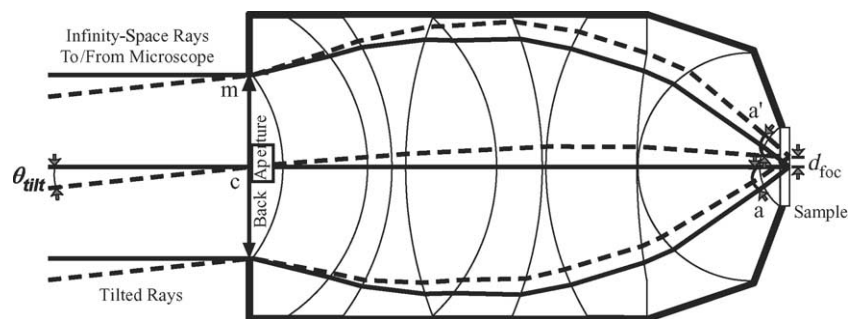


Fig. 3. Cross-sectional view of light rays traveling through an infinity-corrected microscope objective and the errors associate with tilt. Rays traversing the back aperture of the objective at angle  $\theta_{tilt}$ , correspond to a lateral translation of  $\delta_{foc}$  in the sample (Eq. (4)), regardless of the position of the ray in the back aperture. Conversely, rays traversing the back aperture at position  $m$ , correspond to the same aperture angle  $a'$  at the sample, regardless of the position of the ray in the sample. Due to this reciprocal relationship and also since the illumination of the back aperture is uniform, the microscope is largely insensitive to lateral translation between the microscope structural stack and the objective.

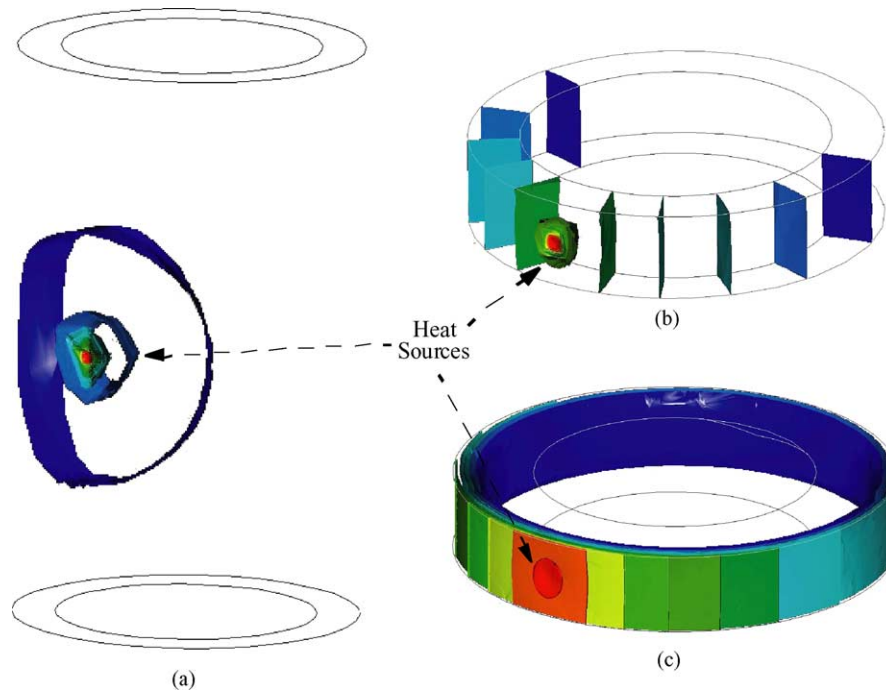


Fig. 4. Steady-state isotherms on (a) long tube, (b) short tube, and (c) insulated and shielded short tube.

cal spot. The mechanical design of the HPM will exploit the translational independence of the infinity-space optics to minimize the sensitive tilt degrees of freedom.

Although the backbone of the microscope is in infinity-space, the sources and detectors in the individual modules are used at finite conjugate. In this case, lenses within the modules focus light from the microscope backbone to a finite conjugate. The light from the infinity-space backbone is also related to the finite conjugate by the Fourier transform so the measurements are also insensitive to translation of the lens relative to the backbone. However, translation motion of these lenses relative to the source or detector within the module will directly couple into the microscope measurements. Fortunately, since the distances between the components at finite conjugate are small, the disturbances are smaller and may be minimized by conventional techniques. For example, the distance between the microscope objective and the sample under observation is at most 2 mm, but more typically 100  $\mu\text{m}$ . Over these distances the translation introduced by the expansion of the microscope structure will be small and may be corrected by position sensing and feedback. Within other units, such as beam expanders, conventional athermalization techniques may be readily used. In contrast, expansion across the long distance of the backbone will be much larger. The larger distances as well as the difficulties of interfacing between modules would make feedback along the backbone more difficult and costly. Hence, using infinity-optics across the backbone is a major advantage while the use of finite-conjugate optics within a module is manageable.

Considering this optical configuration, the segmented HPM structure has two main performance advantages over

a traditional cantilevered or single-tube design. First, as shown by the simulated isotherms in Fig. 4a and b, the axial length of a tube segment affects how heat flows through the tube stack; the ends of the tube present a significant thermal resistance (heat can only escape by natural convection), hence causing a thermal disturbance to flow more readily in the low-resistance path around the circumference of the tube. As a result, the temperature distribution around the circumference of a tube, characterized most simply by the difference in the surface temperature between opposite sides of the tube, is more uniform on a shorter segment. As will be discussed later, the impact of a more uniform temperature distribution on the tilt error depends on the type of disturbance, the dimensions of the segment, and on the material properties of the segment. Nevertheless, when several segments are stacked as in the microscope design, thermal strains in each segment are relieved in the gaps between segments and are transmitted at the locations of the connections between segments.

Each tube segment can be further thermally stabilized by insulating and shielding its surfaces as shown in Fig. 5, with simulated steady-state isotherms shown in Fig. 4c. Here, the inner structural ring is covered by a layer of fiberglass insulation and held in place by a thin shield made by bending metal sheet of high thermal conductivity (e.g., aluminum or copper). Because it is so thin (e.g., 2 mm, giving a very low thermal mass), the shield quickly diffuses temperature gradients around its circumference. The insulation increases the thermal resistance between the outside shield and the structural tube section, ideally providing the isolation that an air gap would give, but without the detriment of natural convec-

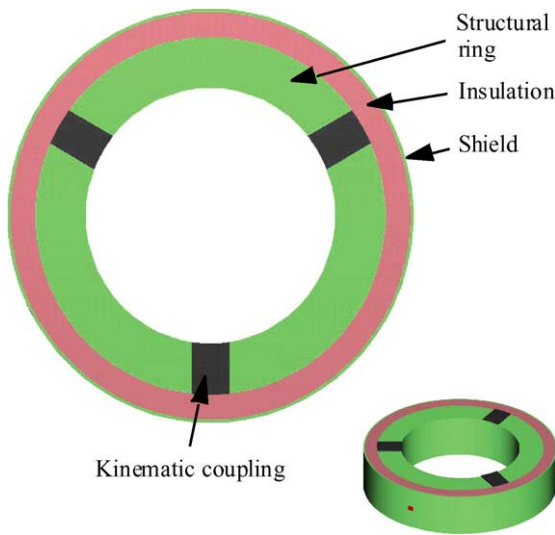


Fig. 5. Cross-section of shielded and insulated tube segment.

tion that has been shown to occur in air gaps larger than a few mm [2]. Machines have been insulated by precision engineers for many years; one recent successful application of adding a shield/insulation barrier was in 1994, when Slocum worked with Flinchbaugh at Weldon Machine Tool to insulate a Model 1632 cylindrical grinder's structure to achieve higher than normal accuracy in a worse than normal shop environment. Furthermore, insulating a structure is a lower-cost alternative to temperature-controlled fluid showers [3], which are not practical for this application.

The second main performance advantage of the HPM is precision mechanical alignment of the optical axes, enforced by the inherent repeatability of the precision-ground “canoe ball”<sup>1</sup> [4,5] kinematic couplings between the segments. Several studies have demonstrated sub-micrometer repeatability of kinematic couplings [4,6–9], and the detailed analysis methods for considering effects such as nonrepeatability due to friction [10] and interchangeability errors due to manufacturing variation [11] are well known. In the HPM design, the equal-angle groove arrangement of the kinematic couplings averages the radial thermal expansion errors of the tubes to minimize the drift of the central optical axis. With the high repeatability of the couplings, the microscope may be rapidly disassembled and assembled while the optical alignment of the system is maintained. The optics within a module will be aligned independently during assembly of the module, using external alignment hardware. Thus, the modules may be used as optical building blocks to reconfigure the microscope for different experiments, eliminating the need for alignment before each experiment.

<sup>1</sup> The “canoe ball”, named as such because it looks like the bottom of a canoe, emulates the spot contact region of a ball as large as one meter in diameter in an element as small as 25 mm across.

### 3. Modeling of thermal errors

Axial thermal expansion of a tube structure due to a temperature gradient around the circumference of the tube causes the tilt error motion shown in Fig. 6. An analytical model of the thermal expansion of the structure necessitates a model of the transient conduction in a tubular geometry, which due to the non-uniformity of heat sources (e.g., diffuse emission from components inside the microscope) and boundary conditions (convection to the ambient), is hardly tractable in closed form. This section presents two alternative approaches: a macroscopic model used to understand the effects of material property trends on the tilt error; and a model of conduction in a single segment treated as a thin plate, used to understand the effect of segment geometry and boundary conditions on the tilt error.

#### 3.1. Macroscopic model

Consider the tube stack drawn in Fig. 6, with a heat source along its left side. In terms of the temperature profiles along the heated ( $T_h$ ) and non-heated ( $T_n$ ) sides (overbars in Eq. (1) denote averages), the differential expansion ( $\delta$ ) between points on opposite sides of the stack is

$$\delta = \alpha_t H (\overline{T}_h - \overline{T}_n) = \alpha_t \left( \int_0^{L_o} (T_h(z) - T_n(z)) dz \right). \quad (1)$$

Hence, the tilt angle ( $\theta_{\text{tilt}}$ ) of the top plate is

$$\theta_{\text{tilt}} = \arctan \left( \frac{\alpha_t H (\overline{T}_h - \overline{T}_n)}{D} \right). \quad (2)$$

The distance ( $\delta_{\text{obj}}$ ) by which the position of the sample moves with respect to the optical backplane where the lasers are

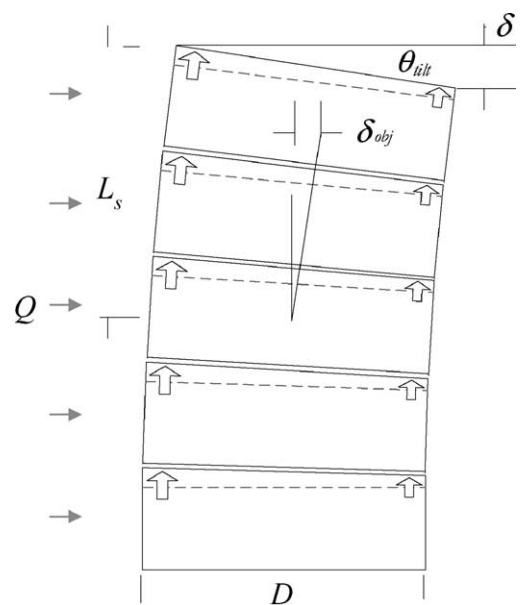


Fig. 6. Tilt error motion caused by circumferentially uneven axial thermal expansion of the tube stack.

Table 1  
Material property, thermal performance index, and critical dimension values for various materials

Material	$\alpha_t$ ( $\mu\text{m}/(\text{m K})$ )	$k$ ( $\text{W}/(\text{m K})$ )	$\rho$ ( $\text{kg}/\text{m}^3$ )	$c_p$ ( $\text{J}/(\text{kg K})$ )	$\alpha$ ( $10^{-6}\text{m}^2/\text{s}$ )	$k/\alpha_t$ ( $\times 10^6$ )	$\alpha/\alpha_t$	$d_{cr}$ (m)
Aluminum (6061)	23.6	185	2700	896	76.5	7.8	3.2	1.68
Copper	17.0	386	8940	385	112.1	22.7	6.6	2.42
Brass	10.3	115	8470	375	36.2	11.2	3.5	1.32
Cast iron (Class 40)	11.0	52	7300	420	17.0	4.7	1.5	0.89
Stainless steel (303)	17.2	16	8000	500	4.0	0.9	0.2	0.49
Silicon carbide	4.4	150	3150	700	68.0	34.1	15.5	1.50
Invar	1.3	10	8050	515	2.4	7.7	1.9	0.39

Properties were gathered from [9,13]. Critical dimensions are based on  $h_c = 2 \text{ W}/(\text{m K})$  and  $w = 13 \text{ mm}$ .

focused at the top of the structure, because the backplane is shifted by the tilt error, is

$$\delta_{\text{obj}} = L_s \frac{\alpha_t H (\bar{T}_h - \bar{T}_n)}{D}. \quad (3)$$

The displacement of the focal spot for an objective of magnification  $M_o$  paired with a tube lens of focal length  $f_T$ , is directly proportional (for small angles) to the tilt angle, through

$$\delta_{\text{foc}} = \left( \frac{1}{M_o} \right) \left( f_T + \frac{f_T}{M_o} \right) \arctan \theta_{\text{tilt}}. \quad (4)$$

Next, we model heat conduction around the circumference of the structure considering a tube segment as a linear body (neglecting convection losses) with effective cross-sectional area  $A = wh$ , effective length  $L = \pi D/2$ , and material thermal conductivity  $k$ . The heat flow  $Q$  through this body is

$$Q = \frac{(\bar{T}_h - \bar{T}_n)}{L} Ak. \quad (5)$$

Eq. (2) thus becomes

$$\delta_{\text{obj}} = \frac{\pi L_s \alpha_t H Q}{2kwh}. \quad (6)$$

Therefore, seeking to minimize  $\delta_{\text{obj}}$  for a chosen structure geometry, the best material for steady-state performance (assuming equal  $Q$ ) is one with maximum thermal conductivity per unit of tendency to thermally expand,  $k/\alpha_t$ .

In terms of transient performance, the penetration depth  $d$  of temperature change through the structure at time  $t$  after a step change in temperature at a boundary is

$$d = \frac{\sqrt{\alpha t}}{\text{Fo}}, \quad (7)$$

where Fo is the Fourier number based on the structure geometry<sup>2</sup> [12], and  $\alpha$  is the material thermal diffusivity.<sup>3</sup> Hence, assuming fixed geometry and fixed  $Q$ , the property ratio  $\alpha/\alpha_t$  is a rough index for maximizing the transient tilt performance. Material properties and steady-state and transient performance indices for various metals and ceramics are listed in Table 1.

<sup>2</sup> For a prismatic body,  $\text{Fo} = 1$  can be assumed to give a rough estimate of the thermal penetration speed.

<sup>3</sup> The thermal diffusivity is the ratio of the thermal conductivity to the product of density and heat capacity ( $a = k/\rho c_p$ ).

From a dimensional analysis of the segmented stack geometry, it is expected that the dimensionless steady-state temperature difference across an individual segment is a function of the aspect ratio of the segment,

$$\frac{(\Delta T)kD}{Q} = f\left(\frac{h}{w}\right). \quad (8)$$

This assumes a constant structure diameter, heat input, and material conductivity, and variable segment thickness  $w$  and height  $h$ . Furthermore, the tilt error of a stack of equal-height segments is a function of the aspect ratio of each segment, and the ratio of the segment height to the total height of the structure ( $H$ ), giving

$$\theta_{\text{tilt}} = f\left(\frac{h}{w}, \frac{h}{H}, \frac{h}{D}\right). \quad (9)$$

The relations from dimensional analysis are used to present design study results in Section 5.

### 3.2. Conduction model for a single segment

The model of heat conduction in a tube can be simplified by “unrolling” the tube into a plate, assuming the radius of the tube is much greater than its thickness, the thickness is much less than the tube height, and that the temperature variation through the thickness is negligible. First, consider the model of a thin circular plate shown in Fig. 7a. To model a localized heat source, a hole in the plate at radius  $r = R_b$  is held at temperature  $T_b$ . No heat transfer occurs across the outer edge of the plate, where  $h_e = 0$ . The differential equation describing the steady-state radial temperature distribution in the plate is

$$r^2 \frac{d^2 T}{dr^2} + r \frac{dT}{dr} - r^2 \frac{h_a}{wk} (T - T_\infty) = 0, \quad T(R_b) = T_b, \\ \frac{dT}{dr}(R_c) = 0. \quad (10)$$

Transforming to dimensionless variables [14], the equation becomes

$$\zeta^2 \frac{d^2 \beta}{d\zeta^2} + \zeta \frac{d\beta}{d\zeta} - \zeta^2 \beta = 0, \quad \theta(Z_b) = 1, \quad \frac{d\beta}{d\zeta}(Z_c) = 0, \quad (11)$$

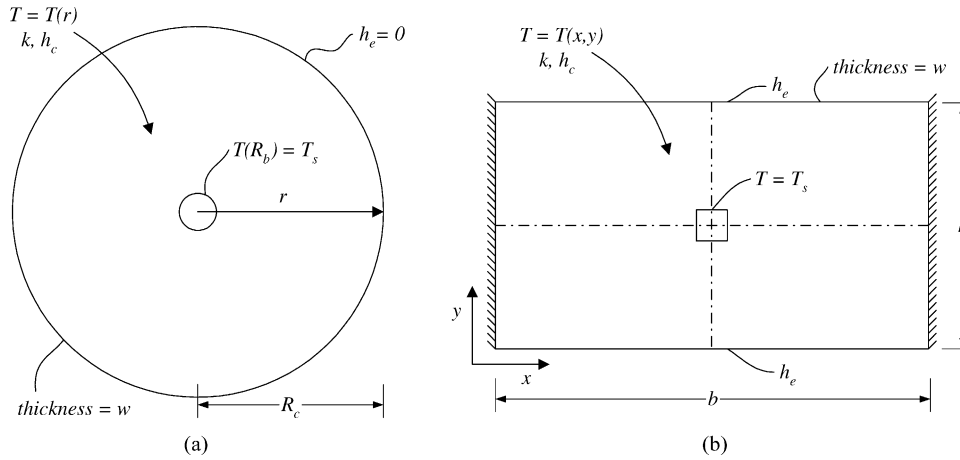


Fig. 7. Two-dimensional heat conduction models: (a) circular plate and (b) rectangular plate.

where

$$\zeta = r \sqrt{\frac{h_a}{wk}}, \quad \beta = \frac{T(z) - T_\infty}{T_b - T_\infty}. \quad (12)$$

The particular solution is a combination of zeroth- and first-order Bessel functions  $I$  and  $K$ ,

$$\beta(\zeta) = \frac{K_1(Z_c)}{I_0(Z_b)K_1(Z_c) + I_0(Z_c)K_1(Z_b)} I_0(\zeta) + \frac{I_1(Z_c)}{I_0(Z_b)K_1(Z_c) + I_0(Z_c)K_1(Z_b)} K_0(\zeta). \quad (13)$$

Now consider the rectangular plate model shown in Fig. 7b, with the convection heat transfer coefficient  $h_e$  along the top and bottom edges representing the constraint against axial heat flow, and the adiabatic side edges reflecting the symmetry (cut line) of the tube. The differential equation for conduction in the plate, with boundary conditions noted in Fig. 7b, is

$$-\left(\frac{\partial^2 T}{\partial x^2} + \frac{\partial^2 T}{\partial y^2}\right) = \frac{h_a}{wk}(T(x, y) - T_\infty) + \frac{1}{\alpha} \frac{\partial T}{\partial t}. \quad (14)$$

This equation was solved numerically using the MATLAB™ PDE Toolbox. When reducing the problem of a thin plate of thickness  $w$  to a generic 2D solution with unit depth, the convection heat transfer coefficient on the outer surface of the plate must be scaled to  $(h_a)_{2D} = 2h_a/w$  to account for the two sides of the plate and for the change in cross-sectional conduction resistance between a thin plate and a plate of unit depth. Note that because of symmetry, the solution region can be reduced to one quadrant of the segment, with adiabatic boundary conditions along the lines of symmetry.

Fig. 8 compares the temperature profiles of the circular and rectangular plate models, under constant flux sources (Fig. 8a) and constant temperature sources (Fig. 8b). Two points are emphasized: first, the plates behave differently ac-

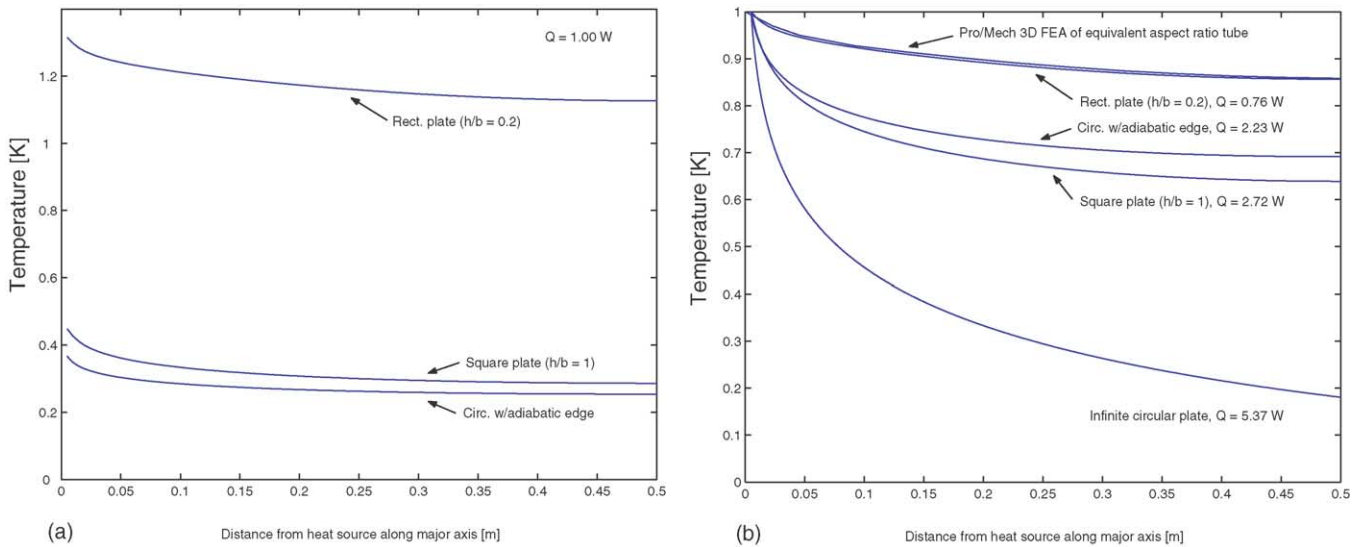


Fig. 8. Comparison of circular plate and rectangular plate conduction models with: (a) constant flux source and (b) constant temperature source.

cording to the source boundary conditions; and second, the constraint the rectangular plate provides against conduction along its minor axis (height dimension) affects the temperature profile along its major axis. Under a constant flux source, the average temperatures of the plates are inversely proportional to their surface area; a plate with a high thermal resistance to the ambient must reach a higher temperature to dissipate the same amount of heat as a plate with a low thermal resistance. Under a constant temperature source, the plate with the smallest area transfers the least heat with the ambient. The rectangular plate, with a height-to-width ratio of 0.2 has a much smaller temperature difference between the extents of its major axis than the square plate (aspect ratio 1.0). This shows that the rectangular segment has temperature uniformity in one direction as a result of restricting conduction in the opposite direction.

The steady-state temperature distribution in a body with fixed<sup>4</sup> boundary conditions and a fixed heat input will be self-similar (dimensionless) with respect to the dimensions of the body and the magnitude of the heat source. Scaling dimensions of the tube segment in the two-dimensional model presented here with a constant heat input will change the temperature of the segment, but not the shape of the temperature distribution. As long as a reasonable temperature change caused by the heat input always reaches the extents of the segment, the tilt angle will not change as the dimensions of the segment change, because the tilt angle is a self-similar quantity with respect to the height of the segment. Conversely, if the effect of the heat input does not reach all extents of the segment, changing the geometry of the segment will considerably affect the tilt error as the segment is shortened and the symmetry of the temperature distribution is broken. Therefore, the thermal penetration depth is a critical dimension for bounding the importance of segmenting a structure. This dimension is estimated by solving Eq. (10) for a circular plate with a very large outer radius,

$$\beta(\zeta) \cong 0.2K_0(\zeta). \quad (15)$$

Defining the penetration depth as where  $\beta = 0.01$  and substituting for  $\zeta$ , the critical dimension value (in meters) is

$$d_{cr} \cong 2.7 \sqrt{\frac{wk}{2hc}}. \quad (16)$$

Hence, if a characteristic dimension of the structure, such as half the circumference of a tube segment, is greater than  $d_{cr}$ , changing the aspect ratio of the segment will significantly change the tilt error. Sample values of the critical dimension for a variety of materials under typical ambient conditions are

<sup>4</sup> The heat transfer coefficient for a vertical plate under natural convection varies with the difference between the surface temperature and ambient temperature as  $(\Delta T)^{1/4}$  [8]. Therefore, the warmer regions of the segment (near the heat source) should lose more heat to the ambient than the cooler regions of the segment (far from the source). Within practical temperature ranges, this assumption may cause about a 5–10% overestimate of the tilt error.

listed in Table 1. Note that this case does not apply to a constant temperature input (although a critical dimension can be found using the heat input derived from a constant temperature boundary condition on a given segment), in which case the total thermal resistance (trending dominantly by segment surface area) of the segment primarily affects the tilt error. This is emphasized further by simulation results presented in Section 5.

### 3.3. Model of shielded section

A two-dimensional model was also built for the tube segment cross-section with insulation and shielding. Considering the cross-section under a localized source as shown in the inset of Fig. 9a, the primary performance goal is for the insulation to delay the transmission of the heat source to the structure (tube) until the shield has conducted the effect of the disturbance fully around the circumference of the structure [1,8]. Hence, an order-of-magnitude criterion for sizing the thicknesses of the shielding ( $w_{sh}$ ) and insulation ( $w_{ins}$ ) guarantees that the thermal resistance against conduction through the insulation is greater than the resistance against conduction around the shield circumference. Considering a heat source on the order of the height of the segment ( $h$ ), the requirement is

$$\frac{w_{ins}}{hk_{ins}} \gg \frac{\pi R}{w_{sh}k_{sh}}. \quad (17)$$

The simulation results in Fig. 9a show that using shielding and insulation can delay the response time to a step input by more than a factor of two, and that the steady-state temperature difference across the shielded and insulated tube is approximately one-tenth of that across the bare tube. Similar results are noted in Fig. 9b for an oscillating input (e.g., ambient cycling due to heating or cooling system); the shielding and insulation both delay and significantly reduce the magnitude of the disturbance on the structural section. Note that heat conduction between the layers was assumed with zero contact resistance; adding contact resistance would increase the positive effect of the shielding and insulation.

### 3.4. Structural finite element models

In addition to the two-dimensional models of the individual segments, three-dimensional finite element models of the stack structures were built in Pro/MECHANICA<sup>TM</sup>. The kinematic coupling balls and grooves between the segments were modeled by sets of 7.5 mm × 7.5 mm rectangular (equal to the Hertz contact area for the preloaded couplings) stainless steel contacts between the tube-to-tube gaps. Consistent with the laboratory test procedure discussed later, square heat sources were placed at the horizontal centerlines of the second, third, and fourth segments of the five-segment structure, and at equivalent positions on the single tube structure. Uniform steady-state heat transfer coefficients, derived from natural convection relations for vertical cylinders and hor-

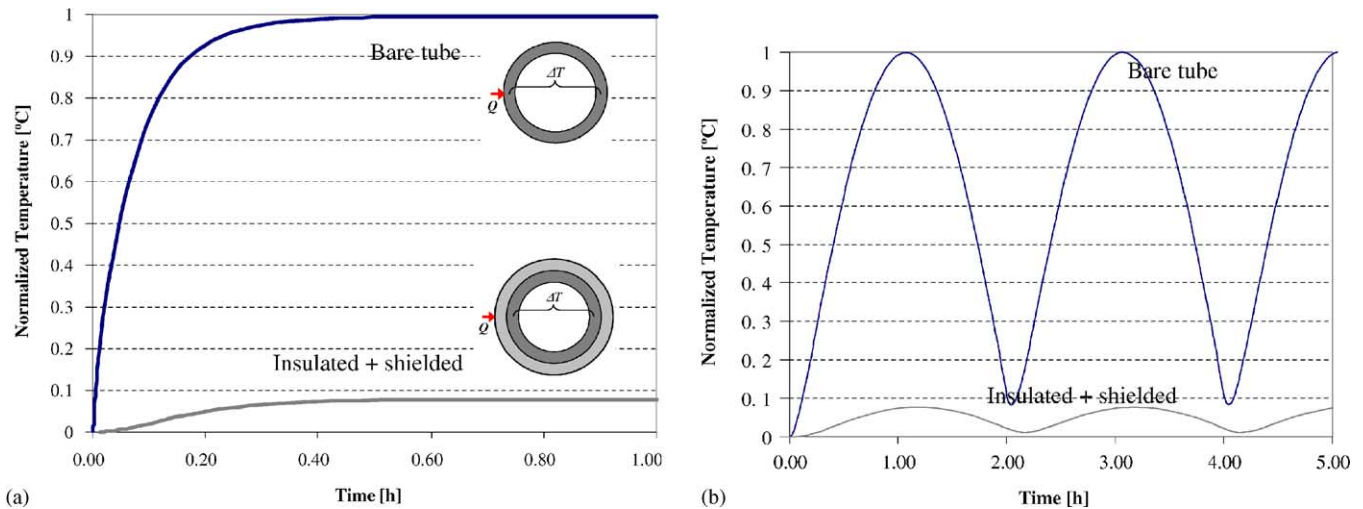


Fig. 9. Average temperature difference across bare and shielded tube cross sections with: (a) step heat input and (b) oscillating heat input  $Q = |\sin(\pi t/2)|$ .

horizontal plates [15], were defined on each external surface of the model. The tilt angle of the structure was calculated using the results of the thermal analysis as a temperature boundary condition for a structural analysis. As shown in Fig. 8a, the steady-state temperature distributions predicted by the Pro/MECHANICA model matched those given by the two-dimensional model solved using the MATLAB PDE toolbox. For practical segment dimensions, the results of the three-dimensional models also justified neglecting the segment curvature and the temperature variation through the thickness of the segment.

## 4. Experiments

### 4.1. Setup and procedure

The thermal stability of the microscope structure was evaluated by applying localized heat inputs to its outside surface, and measuring the resulting circumferential and axial temperature distributions around the tubes, and the tilt angle of the structure with respect to a reference column. Two structures were tested: the five-segment aluminum structure shown in Fig. 10, with 300 mm outside tube diameter, 38 mm wall thickness, 500 mm total height, and 250 mm effective radius stainless steel canoe ball couplings between the segments; and a structure with a single tube having equivalent dimensions to the stack of five segments. Later, each tube was covered with 25 mm thick wrap of fiberglass insulation ( $k = 0.03 \text{ W/(m K)}$ ) and a 2 mm thick aluminum shield.

The temperature distribution on the structures and in the surrounding air was monitored using Minco three-wire platinum RTDs (resistive temperature detectors), with 100  $\Omega$  nominal resistance. Six RTDs spaced equally around the circumference of each tube segment (or at equivalent locations on the single-tube structure) were wired to a National Instruments LabView Data Acquisition System using

SCXI-1322 terminal blocks and SCXI-1122 16-channel multiplexer modules, connected to an SCXI-1000 chassis. The SCXI-1122 modules provided a 1 mA excitation current to each RTD, and 16-bit D/A conversion gave a resolution of 0.006  $^{\circ}\text{C}$ .

The tilt of the structure was measured using a Zygo differential plane mirror interferometer (DPMI) configured for angular measurement [8], mounted to a 125-mm diameter aluminum column placed inside the stack. The DPMI was placed as shown in Fig. 11 and sensed the tilt of a reference mirror mounted to a horizontal plate attached to the top of the tube set. The resolution of the interferometer was 0.06 arcsec.

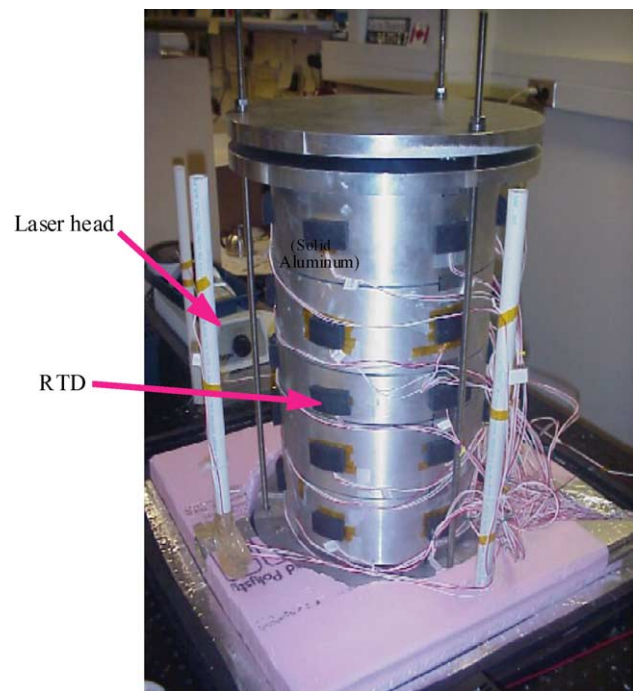


Fig. 10. Prototype of segmented HPM structure.

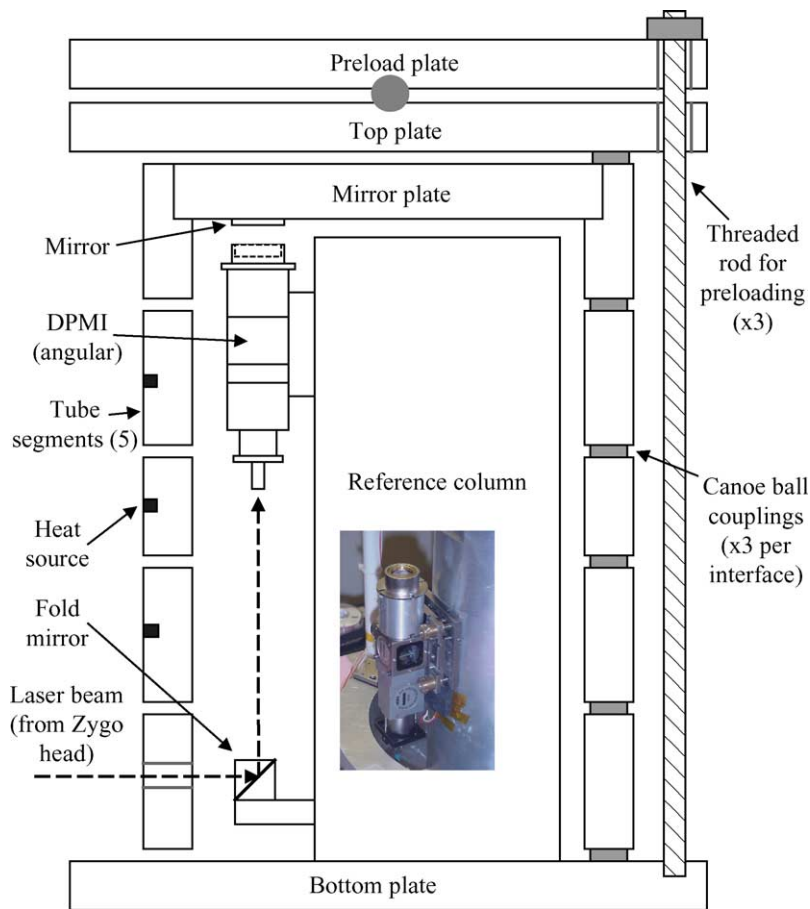


Fig. 11. Tilt metrology setup of tube structure. Inset shows DPMI configured for angular measurement, bolted to reference column.

Thermal disturbances were applied to the structure using Minco copper thin film heating elements, each measuring  $12\text{ mm} \times 12\text{ mm}$ . Three sources were mounted directly to the structure, one each at the vertical midpoints of the three center tubes, aligned vertically parallel to the axis of the interferometer. This placement maximized the ability of the interferometer to capture the gross error motion from thermal expansion, as ideally the maximum differential expansion of the stack was seen by the measurement beams. The sources were wired in a parallel circuit.

The test apparatus (excluding the laser source) was placed in an insulated chamber constructed of 102 mm (4 in.) thick extruded polystyrene (Styrofoam), and mounted on an air-shock isolation table. Single-point readings from the interferometer and each RTD were taken once per minute, with each of two six-hour-long heat input programs starting one hour after data acquisition began: a 3 W (5 V, 0.6 A) step input, and sawtooth waveform with an amplitude of 3 W and a period of 1.5 h. Real heat inputs to a microscope structure may be as small as 0.1 W from precision actuators, or as high as 30 W caused by an operator standing close to a bare structure [1]. Actuators are more likely to represent a constant heat input, where the temperature of the input changes to dissipate the required amount of heat. Conversely, ambi-

ent disturbances from HVAC cycling would be closer to a constant temperature input, because the thermal resistance of the structure would not affect the local air temperature.

#### 4.2. Results

Fig. 12 shows the measured tilt angle of the bare single tube and segmented tube structures, and the insulated and shielded single tube structure. When the heat sources are turned on at  $t = 1\text{ h}$ , the bare structures begin to rapidly drift for the next 40–60 min, and then drift at a much slower rate until the heat sources are turned off near  $t = 7\text{ h}$ . The initial period of drift is more rapid and slightly longer in duration for the single tube structure than for the segmented tube structure; after 120 min, the single tube structure has drifted 0.65 arcsec, while the segmented tube structure has drifted 0.3 arcsec. This shows how the axial conduction resistance provided by the gaps between the tube segments causes the disturbance to more rapidly flow around the structure, and how the gaps between segments relieve thermal strains in the vicinity of the heat source.

Fig. 13 shows the normalized (difference from initial value) temperatures around the circumference of a heated segment of the segmented tube structure, indicating how the

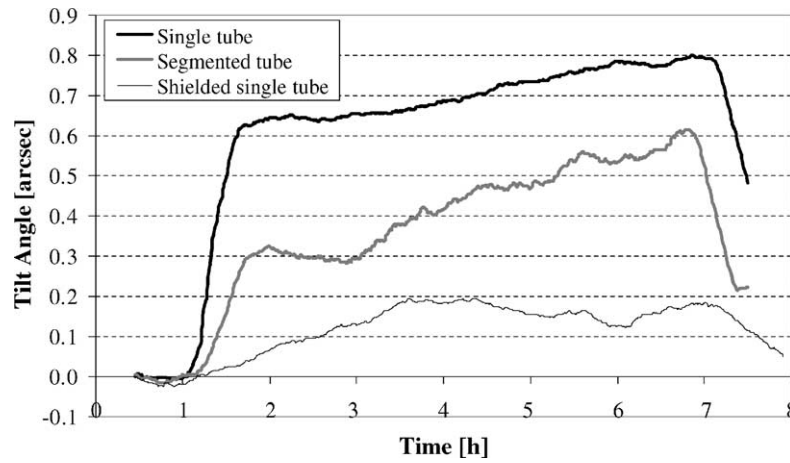


Fig. 12. Measured tilt error of bare one-piece and segmented, and shielded one-piece structures.

temperature change caused by the heat source propagates around the tube. Fig. 14 shows the temperature differences across the segments (differences between sensor readings from positions 1 and 6 on the diagram in Fig. 13) when only the middle segment of the structure is heated. Just like the tilt angle of the structure, the temperature difference across the heated segment increases rapidly during the first hour of heating, and approaches a steady-state value of approximately 0.73 °C near  $t = 3$  h. Furthermore, the temperature differences across the segments that are not heated are negligible throughout the test, indicating that these segments are almost perfectly isolated from the heated segment of the structure and do not contribute to the tilt error. This justifies modeling

the conduction of the segments individually, and (aside from structural stiffness issues) estimating the tilt error using the temperature distributions in the heated segments alone.

Fig. 15 shows temperature measurements from a shielded and insulated segment, with the heat source placed on the outer surface of the shield. The shapes of temperature profiles in Fig. 15 for the surface of the shield resemble those in Fig. 14 for the surface of the bare heated segment; however, the difference among the six measurements on the surface of the tube (underneath the insulation and shielding) is negligible given the measurement resolution. The shielded tube maintains almost perfect temperature uniformity while it is heated, and it is heated much more slowly and to a lower fi-

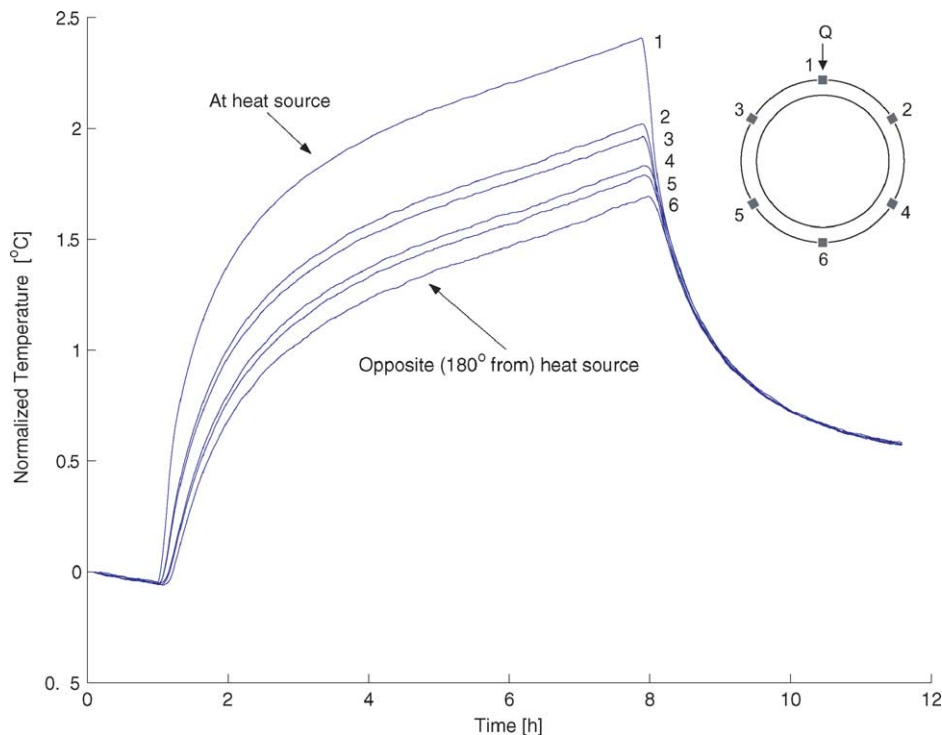


Fig. 13. Measured temperatures on heated segment of segmented tube structure.

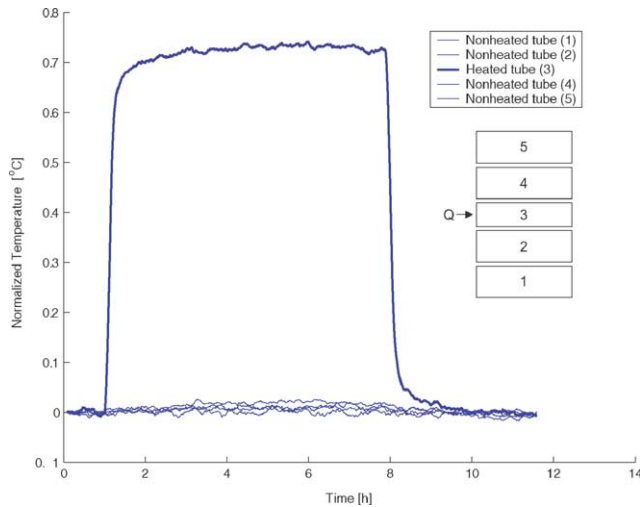


Fig. 14. Measured temperature differences across segmented tube structure.

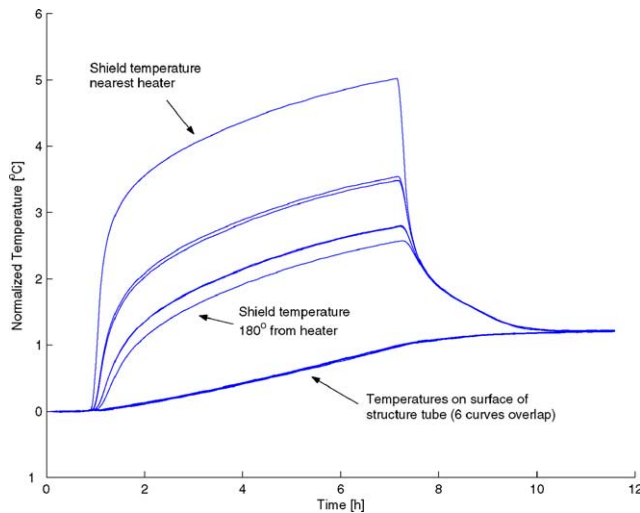


Fig. 15. Comparison of temperatures on surface of heated shielding and on surface of structural tube.

nal temperature than the comparable bare tube. Note also that the shield reaches much higher temperatures than the bare heated tube, which makes sense because the thin shield has a much smaller thermal mass and a much larger cross-sectional thermal resistance than the tube segment.

Considering observations from both the temperature measurements and the drift measurements, a reasonable estimate of the steady-state tilt error of the structure is the value at  $t = 3$  h, when the temperature differences at the heated level reach steady-state. At this time, the segmented tube structure has tilted 0.35 arcsec, the tilt of the single tube structure is 0.65 arcsec, and the tilt of the shielded single tube structure is 0.20 arcsec. The increase in the tilt of the structures after 4 h is likely due to drift<sup>5</sup> of the interferometer, caused in part by

<sup>5</sup> The stability range of the interferometer while isolated in the styrofoam chamber, under ambient fluctuations caused by the HVAC system in the lab, was measured to be approximately 0.10 arcsec.

transmission of the temperature gradient from the heated areas to the column<sup>6</sup> supporting the interferometer, via the air inside the stack enclosure. Note that tilt measurements from the shielded and segmented tube structure fell completely within the stability limit of the interferometer and as a result are not presented.

The Pro/MECHANICA finite element models predicted 0.40 arcsec tilt of the segmented tube structure and 0.60 arcsec tilt of the single tube structure, both within 20% of the measured estimates. This difference could be caused by the assumption of uniform convection losses and slight errors in modeling of the coupling contacts. More specifically, Table 2 compares the measured and simulated temperature differences at each tube centerline level for both structures, when heat sources are placed on the second, third, and fourth segments, or at equivalent levels on the single tube. These differences are within 0.03 °C at all levels of both structures. Simulations of the shielded structures predicted tilt values much less than those measured using the interferometer—0.037 arcsec for the segmented tube and 0.054 arcsec for the single tube. Both of these values are below the minimum reading of the interferometer, as well as its drift under ambient fluctuations. Since the temperature measurements showed that the shielding almost perfectly isolates the structure tubes from the heat sources, meaning that the tubes expand axially with very little tilt error compared to a bare structure, it is reasonable to trust the simulation results as the best estimates for the shielded structures.

## 5. Design studies

Validation of the finite element models using the measurements from the single tube and segmented aluminum structures permitted their use for design studies to evaluate the effects of segment aspect ratio, boundary conditions, and material properties on the tilt error. First, Fig. 16 shows the transient tilt error for segments under a constant temperature source, with width  $b = 1$  m, thickness  $w = 25$  mm, and height ranging from  $h = 50$  mm to  $h = 1$  m. The tilt angle first increases sharply, as the disturbance propagates along the minor axis of the segment near the source, and then contracts as the disturbance reaches the opposite side of the segment and the temperature distribution approaches steady-state. Note that time to reach steady-state is proportional to the segment height, while the relative magnitude of the transient “overshoot” is approximately constant. Fig. 17 shows how the steady-state tilt error varies with segment aspect ratio for a variety of segment widths. Here, the tilt error is directly related to the total surface area of the segment, and hence is inversely related to the thermal resistance of the

<sup>6</sup> However, within the first hours of test, temperatures on the support column were uniform within 0.1 °C, compared to a typical difference of 1–2 °C around the circumference of a heated tube, so the column was considered a stable reference for mounting the interferometer for tilt measurement.

Table 2  
 Simulated and measured steady-state temperature differences (°C) across segmented and single tube structures with three heat sources

Level (1: bottom)	Simulated $\Delta T$ across segmented tube	Measured $\Delta T$ across segmented tube	Simulated $\Delta T$ across single tube	Measured $\Delta T$ across single tube
1	0.01	$0.00 \pm 0.01$	0.07	$0.06 \pm 0.01$
2	0.12	$0.13 \pm 0.02$	0.12	$0.09 \pm 0.02$
3	0.18	$0.21 \pm 0.03$	0.12	$0.12 \pm 0.01$
4	0.12	$0.12 \pm 0.02$	0.12	$0.09 \pm 0.02$
5	0.01	$0.00 \pm 0.01$	0.07	$0.06 \pm 0.01$

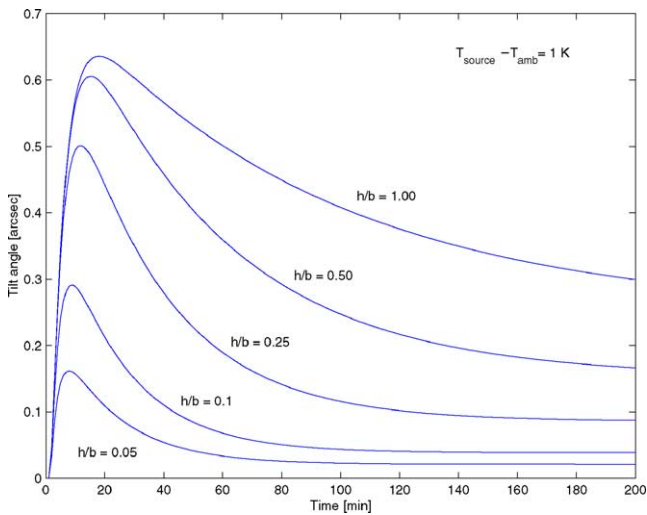


Fig. 16. Simulated tilt angle vs. time for segments of various aspect ratios, with a constant temperature source.

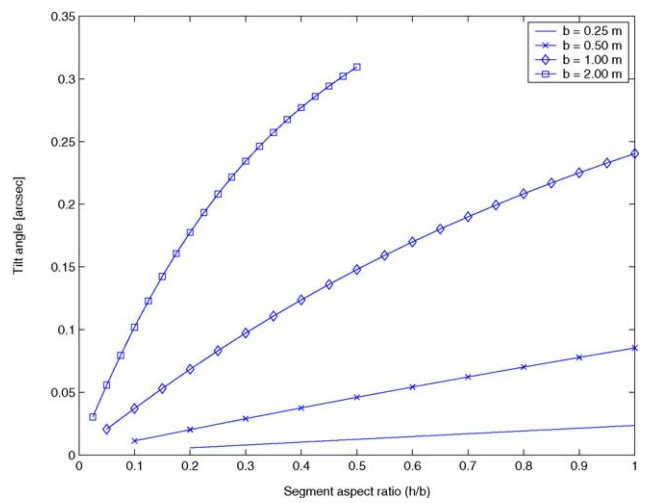


Fig. 17. Simulated steady-state tilt angle vs. segment aspect ratio, for various segment widths, with a constant temperature source.

segment. Therefore, if a tubular structure will experience a localized constant temperature disturbance, segmenting the structure in the vicinity of the disturbance will always reduce the tilt error.

However, the behavior of a tube segment under a constant flux disturbance differs considerably from the behavior under a constant temperature disturbance. As was derived in Section 3, the steady-state thermal penetration distance for

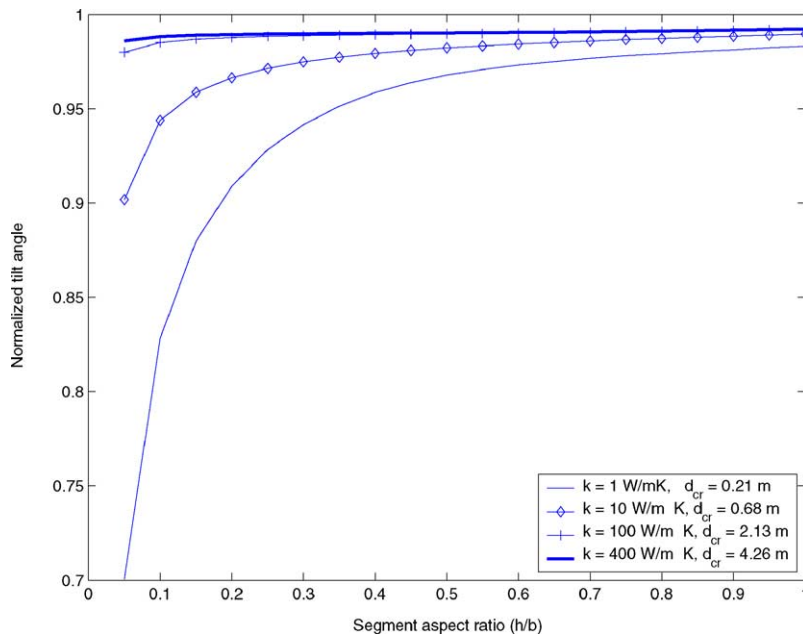


Fig. 18. Effect of thermal conductivity on steady-state tilt error of segments of varying aspect ratio, with a constant flux source.

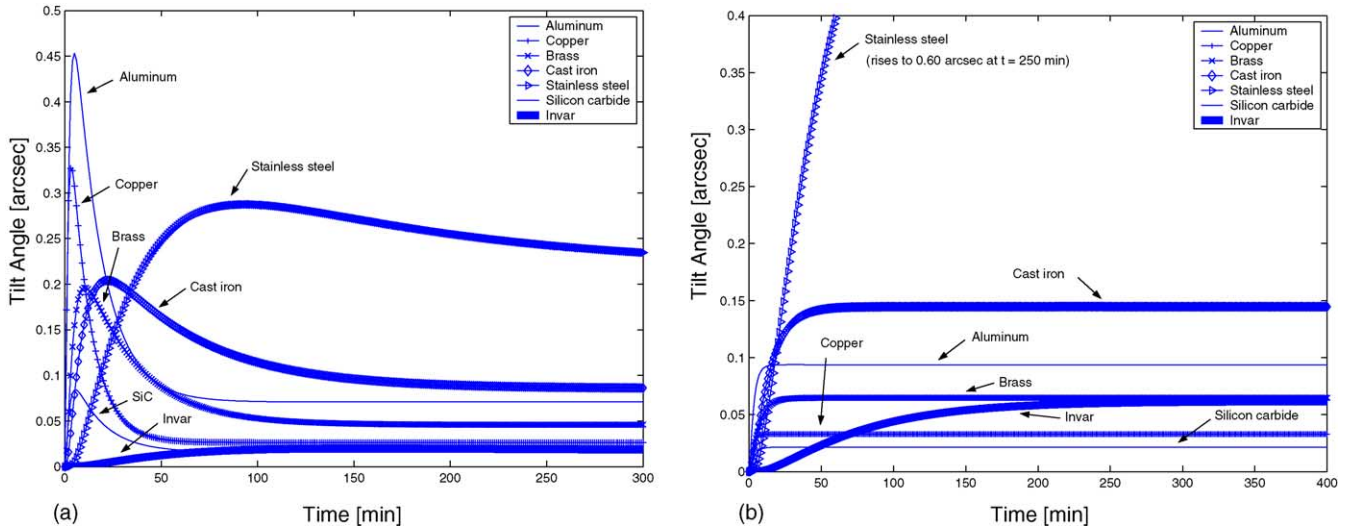


Fig. 19. Transient tilt error for common structural materials: (a) constant temperature source and (b) constant flux source.

conduction in a thin plate can be used to roughly determine whether or not segmentation of a tube subject to a localized constant flux disturbance will affect the tilt error. This effect is emphasized in Fig. 18, which shows the steady-state tilt error versus aspect ratio for segments of half-width  $b/2 = 1.0$  m, with varying thermal conductivity. Values of the critical dimension, calculated using Eq. (16), are listed in the legend. When the width of the segment is less than the critical value (for  $k = 100, 400$ ), changing the aspect ratio negligibly affects the tilt error; conversely, when the width of the segment exceeds the critical value (for  $k = 1, 10$ ), reducing the height of the segment considerably reduces the tilt error because the thermal disturbance reaches the edge constraints of the model.

Because the critical dimension rule is derived from a one-dimensional distribution, it best applies to structures for which a thin-plate equivalent can be established. In the specific case of a thin-walled tube, it seems that the largest dimension of heat conduction within the tube, such as the half-width (half of the equivalent circumference), is the appropriate characteristic dimension. Furthermore, the tilt error of a segment with aspect ratio greater than one (e.g., a long, thin tube) seems to be insensitive to all constant flux disturbances, because the circumferential conduction path becomes shorter than the axial path. Assuming the critical dimension rule is met, significant reduction of tilt error under a constant flux disturbance will only occur if a tube is segmented into relatively short, wide sections.

Next, the rectangular plate model was solved with fixed geometry ( $h = 0.2$  m,  $w = 0.013$  m,  $b = 1$  m) for a variety of materials, giving the results in Fig. 19. In both cases, stainless steel and cast iron give the greatest steady-state tilt errors, while silicon carbide gives the least tilt error. Owing to its high thermal diffusivity, copper has the fastest transient response to a step change in temperature, while Invar has the slowest transient response because of its low thermal

conductivity. Note that Invar, which is traditionally sought for thermal isolation because of its extremely low coefficient of thermal expansion, has nearly the same tilt error under a constant temperature disturbance as silicon carbide; however, under a constant heat flux Invar has over twice the tilt error of silicon carbide, because its low thermal conductivity restricts the disturbance from penetrating the full area of the segment. This is also confirmed by noting that the tilt error of the Invar segment does not exhibit the transient “overshoot” under a constant temperature source; the  $d_{cr}$  value of 0.39 m listed in Table 1 for Invar is less than half the width of the segment modeled. Hence, segmenting the Invar section will considerably reduce its tilt error.

Considering the experimental results from the aluminum tube structures in light of the trends predicted by simulation, it is apparent that the test conditions represented a mixture of the constant temperature and constant flux boundary conditions modeled analytically, for fully thermally penetrated segments. Returning to Fig. 12, the step response of a single tube structure is representative of a segment under a constant flux source, while the apparent slight overshoot in the response of the segmented structure is characteristic of a constant temperature input. The gaps in the segmented structure clearly relieved significant thermal strains between the segments. A small overshoot in the tilt of the single tube structure may have been masked by drift of the interferometer. Measurement of the tilt error using a more sensitive and more thermally stable measurement system would help to more accurately compare the measured results to transient simulations.

Furthermore, the two-dimensional conduction models do not consider the effect of structural stiffness on the transmission of tilt errors between segments, as emphasized by Fig. 20. The gaps between the segments of the prototype structure relieved thermal strains in the vicinity of the heat sources and reduced the tilt error because the sources were

placed circumferentially between the kinematic couplings. If the sources were placed in line with the kinematic couplings, the strains near the heat sources would be transmitted between the segments, and the difference between the tilt errors of the segmented and single tube structures would diminish; the segmented structure would behave similarly to a single-tube structure assembled by welding strips of insulating material between the segments. Finite element simulations with the sources aligned with the couplings predict 0.56 arcsec tilt of the segmented structure and 0.70 arcsec tilt of the single tube, about half the relative difference that occurred with the sources away from the couplings. Furthermore, as the ratio of the tube height to diameter decreases, the advantage of segmentation in locally relieving the thermal strains increases. Nevertheless, the advantages of segmentation based solely on the heat conduction analysis prevail, independent of the source locations. The greatest gain would come under a localized constant temperature disturbance placed at the maximum distance from the coupling locations; while the least gain would arise with a diffuse constant flux disturbance located near the couplings. Further investigation into the effects of source placement and the differences between diffuse and localized disturbances is necessary.

As a final comparison, Table 3 presents the error motions for a variety of HPM structure configurations. The translation values are calculated using Eqs. (3) and (4), with the dimensions of the aluminum prototype. The advantages of segmenting the structure, adding insulation, and adding insulation with shielding superimpose in an approximately

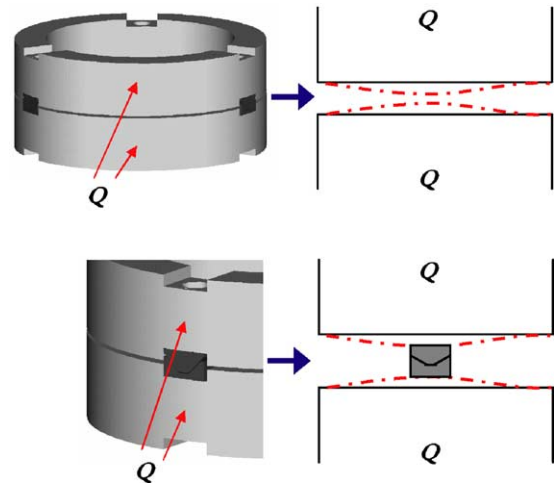


Fig. 20. Schematic effect of source placement on transmission of thermal strains between segments.

linear fashion. Furthermore, the advantages gained by appropriately scaling the segment geometry are overcome by the benefits of adding shielding and insulation to the structure. Installing segmented shielding on a monolithic structure, perhaps using an insulation blanket wrapped with sections of copper wire or thin copper plate, would provide significant thermal benefit even if the modularity offered by kinematic couplings or other precision locators is not needed. All in all, segmentation, shielding, and appropriate choice of ma-

Table 3

Predicted steady-state thermal drifts at microscope objective for single tube and segmented tube designs using various material combinations and dimensions of prototype HPM structure

Structure	Insulation	Shield	Tilt (arcsec)	Translation of top plate (nm)	Displacement of focal spot (nm)	
Design	Material					
Single tube	Aluminum	–	–	(*) 0.65	788	8.1
	Aluminum	Foam	–	0.14	173	1.8
	Aluminum	Foam	Aluminum	0.06	69	0.7
	Aluminum	Foam	Copper	0.03	40	0.4
	Cast iron	–	–	1.03	1249	12.9
	Copper	–	–	0.21	258	2.7
	Invar	–	–	0.47	564	5.8
	Si carbide	–	–	0.16	190	2.0
	Segmented	Aluminum	–	–	(*) 0.35	424
Aluminum		Foam	–	0.09	108	1.1
Aluminum		Foam	Aluminum	0.04	44	0.5
Aluminum		Foam	Copper	0.02	25	0.3
Cast iron		–	–	0.63	768	7.9
Cast iron		Foam	Copper	0.03	39	0.4
Copper		–	–	0.13	157	1.6
Copper		Foam	Copper	0.01	8	0.1
Invar		–	–	0.25	304	3.1
Invar		Foam	Copper	0.03	31	0.3
Si carbide		–	–	0.10	117	1.2
Si carbide		Foam	Copper	0.01	5	0.1

Values marked with (\*) were measured, and all other values were scaled linearly from values obtained by simulation, based on the discrepancy between simulation values and measured values for the measured configurations. Note that while the optics and detection electronics could resolve motions as small as 0.01 nm, some of the smallest thermal errors (e.g., 0.1 nm) would likely be swamped by the positioning error of the stages.

materials can reduce the error motion by up to two orders of magnitude, making nanometer-scale thermal stability of a meter-scale tubular structure a realistic goal.

## 6. Conclusion

This study demonstrates the feasibility of a segmented design for modular instrumentation structures such as microscopes. Reducing the model of conduction in a tube segment from a three-dimensional problem (requiring a lengthy FEA simulation) to a suitable two-dimensional equivalent (which could be solved in a few seconds using MATLAB™), gives good insight into the important design parameters. Methods of reduced-order conduction modeling for shielded structures can also be investigated, such as the thin-layer method presented by Park [16].

The analysis of the HPM design confirms that if the disturbances are localized, the critical dimension rules presented here can be used to determine the best segment size. Kinematic couplings can be excellent thermal isolators between segments, but perhaps a greater benefit of segmentation is the maintenance of structural integrity while offering the flexibility of disassembly, reconfiguration, and reassembly. When thermal disturbances are not directly coupled to the structure, using insulation and shielding most significantly improves the thermal performance, making it possible to isolate existing structures made of conventional materials at a reasonable cost.

## Acknowledgments

John Hart is grateful for the support of a National Science Foundation Graduate Research Fellowship, a Fannie and John Hertz Foundation Fellowship, and the Ford-MIT alliance. Matt Sweetland designed the segmented stack. Jason Sutin's work and construction of the prototype structures were funded by National Center for Research Resources-National Institutes of Health Grant PHS 5 P41 RR03155. Philip Loiselle and Way Luu helped machine, assemble, wire, and test the prototype structures, which

were procured using funds from the NIH grant. Way's work was supported by the Ralph L. Evans Endowment Fund for undergraduate research at MIT. Finally, the authors thank Theo Ruiji and his colleagues from Philips for their suggestions about thermal shielding and the effects of source placement.

## References

- [1] Pluta M. *Advanced light microscopy: principles and basic properties*. Amsterdam: Elsevier Science; 1992.
- [2] Ruiji T. *Ultraprecision coordinate measuring machine*. Ph.D. Thesis, Eindhoven, The Netherlands; 2001. p. 31.
- [3] Debra DB, Bryan JB. Shower and high pressure oil temperature control. *Ann CIRP* 1986;35(1):359–63.
- [4] Mullenheld B. *Prinzipien der kinematischen Kopplung als Schnittstelle zwischen Spindel und Schleifscheibe mit praktischer Erprobung im Vergleich zum Kegel-Hohlschaft* (Translation: application of kinematic couplings to a grinding wheel interface). S.M. Thesis, University of Aachen, Germany; 1999.
- [5] Hart AJ. *Design and analysis of kinematic couplings for modular machine and instrumentation structures*. S.M. Thesis, Department of Mechanical Engineering, Massachusetts Institute of Technology; 2001.
- [6] Slocum AH, Donmez A. Kinematic couplings for precision fixturing—part 2: experimental determination of repeatability and stiffness. *Prec Eng* 1988;10:115–22.
- [7] Slocum AH. Design of three-groove kinematic couplings. *Prec Eng* 1992;14:67–76.
- [8] Poovey T, Holmes M, Trumper DL. A kinematically-coupled magnetic bearing test fixture. *Prec Eng* 1994;16:99–108.
- [9] Slocum AH. *Precision machine design*. Society of Manufacturing Engineers; 1992. p. 304–420.
- [10] Hale LC, Slocum AH. Optimal design techniques for kinematic couplings. *Prec Eng* 2000;25:114–27.
- [11] Hart AJ, Slocum AH, Willoughby P. Kinematic coupling interchangeability. *Prec Eng* 2004;28:1–15.
- [12] Lienhard IV JH, Lienhard V JH. *A heat transfer textbook*. 3rd ed. Cambridge, MA: Phlogiston Press; 2003. p. 195.
- [13] MatWeb material property data, <http://www.matweb.com>, results of database searches.
- [14] Mills AF. *Heat transfer*. Englewood Cliffs, NJ: Prentice-Hall; 1999. p. 101.
- [15] Kaviany M. *Principles of heat transfer*. Course reader for mechanical engineering 370, University of Michigan at Ann Arbor, 1999, p. 538.
- [16] Park J. *Wave motion in finite and infinite media using the thin-layer method*. Ph.D. Thesis, Department of Civil and Environmental Engineering, Massachusetts Institute of Technology, 2002.